Journal of Materials Chemistry B

PAPER

View Article Online
View Journal | View Issue

Cite this: J. Mater. Chem. B, 2024, 12, 3509

A copper-loaded self-assembled nanoparticle for disturbing the tumor redox balance and triple anti-tumor therapy†

Jieli Yin,‡[a] Chen Liu,‡[a] Jiaqi Guo,[a] Mao Li,[a] Baoyin Chen,[a] Xuewen Zhang,[a] Bing Wang,[b] Xuan Zhu*[a] and Dengyue Chen *[a]

Received 31st October 2023,
Accepted 8th March 2024

DOI: 10.1039/d3tb02576d

rsc.li/materials-b

Both chemodynamic therapy and photodynamic therapy, based on the production of reactive oxygen (ROS), have excellent potential in cancer therapy. However, the abnormal redox homeostasis in tumor cells, especially the overexpressed glutathione (GSH) could scavenge ROS and reduce the anti-tumor efficiency. Therefore, it is essential to develop a simple and effective tumor-specific drug delivery system for modulating the tumor microenvironment (TME) and achieving synergistic therapy at the tumor site. In this study, self-assembled nanoparticles (named CDZP NPs) were developed using copper ion (Cu^{2+}), doxorubicin (Dox), zinc phthalocyanine (ZnPc) and a trace amount of poly(2-(di-methylamino)ethyl-methacrylate)–poly[(*R*)-3-hydroxybutyrate]–poly(2-(dimethylamino)ethylmethacrylate) (PDMAEMA–PHB–PDMAEMA) through chelation, π–π stacking and hydrophobic interaction. These triple factor-responsive (pH, laser and GSH) nanoparticles demonstrated unique advantages through the synergistic effect. Highly controllable drug release ensured its effectiveness at the tumor site, Dox-induced chemotherapy and ZnPc-mediated fluorescence (FL) imaging exhibited the distribution of nanoparticles. Meanwhile, Cu^{2+}-mediated GSH-consumption not only reduced the intracellular ROS elimination but also produced Cu^{+} to catalyze hydrogen peroxide (H_2O_2) and generated hydroxyl radicals ($^{\bullet}OH$), thereby enhancing the chemodynamic and photodynamic therapy. Herein, this study provides a green and relatively simple method for preparing multifunctional nanoparticles that can effectively modulate the TME and improve synergetic cancer therapy.

Introduction

Cancer remains a serious condition affecting human health worldwide.[1–3] Conventional cancer therapies, such as surgery, chemotherapy, and radiotherapy display limited therapeutic effects and often lead to severe side effects.[4,5] Recently, novel emerging strategies, including photodynamic therapy (PDT), sonodynamic therapy (SDT) and chemodynamic therapy (CDT), have been significantly applied in precise cancer therapy due to their relatively low toxicity toward normal cells.[6–9] PDT, as a non-invasive strategy for cancer therapy, requires photosensitizers, molecular oxygen and laser-stimulation to generate singlet oxygen ($^1O_2$), which can destroy lipids, proteins and nucleic acids, ultimately leading to tumor cell death.[10,11] Similarly, SDT-mediated toxicity is based on the generation of reactive oxygen (ROS) *via* ultrasound (another exogenous trigger), oxygen and sonosensitizers.[12,13] Additionally, CDT, as a novel-emerging strategy, is a ROS-mediated therapy which catalyzes hydrogen peroxide (H_2O_2) to generate highly reactive hydroxyl radicals ($^{\bullet}OH$) through a Fenton or Fenton-like reaction.[14–16]

Nevertheless, the complicated tumor microenvironment (TME) poses great challenges for current cancer therapy strategies.[17,18] One of the major factors is the antioxidant defense system, mainly attributed to the overexpressed glutathione (GSH) in tumor cells that can regulate the oxidative stress and bring anticancer drug resistance.[19,20] In particular, GSH, an important antioxidative molecule and one of the biomarkers overexpressed in cancer, has the ability to scavenge ROS and result in the reduction of ROS-related therapeutic efficiency.[21,22] Therefore, GSH-depletion agents show promise as a potential strategy to enhance the efficiency of anticancer therapeutics. For example, Liu *et al.* reported FeCo/Fe–Co DAzyme/PL mediated multiple ROS storms, GSH/GPX4 depletion, LOX catalysis, and IFN-γ-mediated ACSL4 activation for irreversible

[a] School of Pharmaceutical Sciences, Xiamen University, Xiamen, Fujian, 361102, China. E-mail: zhuxuan@xmu.edu.cn, dchen@xmu.edu.cn
[b] College of Environmental Science and Engineering/Sino-Canada Joint R&D Centre for Water and Environmental Safety, Nankai University, Tianjin 300071, P. R. China

† Electronic supplementary information (ESI) available. See DOI: https://doi.org/10.1039/d3tb02576d

‡ J. L. Y. and C. L. contributed equally to this work.

cascade immunogenic ferroptosis.[23] With the development of nanotechnology, the integration of GSH-depletion agents with other therapies (SDT, CDT or PDT) to prepare synergistic nanomedicines has been widely developed recently.[24–27] Cheng *et al.* constructed iron-rich mesoporous dopamine (MPDA@Fe) nanovehicles, which facilitate the dual depletion of GSH by both Fe and MPDA. This synergistic action enhances lipid peroxidation and enables the induction of ferroptosis.[28] Sun *et al.* developed perovskite-type manganese vanadate ($MnVO_3$) sonosensitizers that could effectively produce ROS. At the same time, it had a good CDT effect under acidic conditions. In addition, due to the presence of high-valent vanadium, it could effectively consume GSH, thereby synergistically enhancing CDT and SDT.[29] Wu *et al.* reported a second near-infrared (NIR-II) photoactivatable enzyme-loaded nanomedicine (LCG, liposome-Cu-GOx nanocarriers) for effective and safe cancer therapy by PTT and CDT.[30] In addition, Li *et al.* achieved dynamic Cu^{2+}/Cu^{+} circulation through the co-delivery of Cu^{2+} and glucose oxidase (GOD). This approach addresses the challenge posed by the overexpressed GSH and inadequate endogenous H_2O_2 levels in tumors, thereby enhancing the efficiency of copper ions in catalyzing a Fenton-like reaction and improving the efficiency of the CDT effect.[31] Combining UCNPs with rare earth luminescent materials to construct a theranostic nanoplatform is an important strategy for synergistic effects.[32] Zhang *et al.* developed small-sized upconversion nanoparticles (UCNPs). In this system, MnO_2 exhibited excellent glutathione peroxidase (GPx)-like activity, effectively decomposing intracellular over-expressed GSH and further enhancing the therapeutic effect.[33] To sum up, metals in an oxidation state not only reduce the levels of GSH but also generate metal ions in a reduction state, contributing to the production of hydroxyl radicals ($^{\bullet}OH$).

Moreover, Cu^{+}-catalyzed Fenton-like reactions demonstrated a higher efficiency compared to Fe^{2+} in weakly acidic media.[34–36] Within a living organism, copper is connected to ligands such as protein, and an excess of free copper can potentially cause serious toxicity.[37,38] Consequently, it is essential to develop nanoparticles that ingeniously integrate Cu^{2+} with mainstream therapeutics and spatiotemporally confine active agents in the tumor site. Recent research studies have explored the utilization of biocompatible carriers for delivering metal ions or metallic oxides to the tumor site, albeit with challenges such as limited drug loading rate, complex preparation processes and potential toxicity from excipients.[39,40] Noncovalent interactions (π–π stacking, hydrophobic and so on) have been employed to prepare environment-responsive self-assembled nanoparticles which could eliminate unexpected toxicity, avoid complex chemical conjugation and alter drug structure. Hence, considering that copper ions have the ability to coordinate with ligands containing phenolic hydroxyl group, self-assembled nanoparticles were developed (named CDZP NPs) using copper ion (Cu^{2+}), doxorubicin (Dox), zinc phthalocyanine (ZnPc) and a trace amount of poly(2-(di-methylamino)ethylmethacrylate)–poly-[(*R*)-3-hydroxybutyrate]–poly(2-(dimethylamino)ethylmethacrylate) (PDMAEMA–PHB–PDMAEMA) through an assembled procedure. The prepared nanosystem not only exhibited ZnPc-mediated fluorescence (FL) imaging but also demonstrated an enhanced synergistic therapeutic effect involving chem/chemodynamic/phototherapy through GSH-depletion specifically in the tumor site. To begin with, CDZP NPs are capable of accumulating at the tumor site through the enhanced permeability and retention (EPR) effect upon intravenous injection. Subsequently, they are taken up by cancer cells, releasing reactive substances under the stimulations of GSH/pH/laser. The released Dox hampers the function of topoisomerase II, leading to the destruction of cancer cells. Meanwhile, ZnPc could exert phototherapy effects under laser irradiation, encompassing photothermal therapy (PTT) that released heat and photodynamic therapy that generated singlet oxygen ($^1O_2$). Furthermore, Cu^{2+} contributed to GSH conversion into GSSG and generated Cu^{+} to react with H_2O_2, resulting in ROS-mediated CDT. The depletion of GSH could enhance ROS-based therapy, containing CDT as well as PDT effects. Therefore, this multifunctional nanoparticle could effectively regulate the redox levels in the tumor site and enhance the synergistic effect of chemotherapy, phototherapy and chemodynamic therapy.

Materials, cell lines and animals

$Cu(CH_3COO)_2{\cdot}H_2O$ was purchased from Zhengzhou Xipaike Technology Co., Ltd (China). Doxorubicin hydrochloride was purchased from Shanghai Macklin Biochemical Co., Ltd (China). Zinc phthalocyanine (ZnPc), *N*,*N*-dimethylformamide (DMF), triethylamine, methanol, 9,10-anthracenediyl-bis (methylene)-dimalonic acid (ABDA), glutathione (GSH), and 5,5′-dithio bis-(2-nitrobenzoic acid) (DTNB) were purchased from Aladdin (China). Poly(2-(di-methylamino)ethylmethacrylate)–poly[(*R*)-3hydroxybutyrate]–poly(2-(di-methylamino)ethylmethacrylate) (PDMAEMA–PHB–PDMAEMA) was provided by Singapore Polytechnic, School of Chemical & Life Sciences.[41] Hydrogen peroxide (H_2O_2) was purchased from Xilong Science Co. Ltd (China). Dulbecco's modified Eagle's medium (DMEM) was purchased from HyClone (USA). 4′,6-Diamidino-2-phenylindole (DAPI) was purchased from Sigma (USA). Methyl thiazolyl tetrazolium (MTT) and the GSH detection kit were purchased from Beijing Solarbio Science & Technology Co., Ltd (China). The reactive oxygen (ROS) detection kit, 3,3′,5,5′-tetramethylbenzidine (TMB), penicillin–streptomycin solution, trypsin, and 2,7-dichlorodihydrofluorescein diacetate (DCFH-DA) were purchased from Beyotime Institute Biotechnology. The apoptosis kit and live/dead cell staining kit were purchased from Yeasen Biotechnology (Shanghai) Co., Ltd (China).

HeLa cells and 4T1 cells were obtained from American Type Culture Collection (ATCC, MD, USA). BALB/c nude mice were provided by Xiamen University Laboratory Animal Center. 4T1 tumor-bearing mice models were established by subcutaneous injection of 4T1 cells (1×10^6 cells in 100 μL of PBS) into the right hindlimb of mice. When the tumor volume reached 100–200 mm^3, mice were used for subsequent experiments. All animal experiments were carried out in accordance with the

regulations of the Institutional Animal Care and Use Committee of Xiamen University.

Synthesis of doxorubicin (Dox), Cu-Dox (CD), Cu-Dox-ZnPc (CDZ) and Cu-Dox-ZnPc modified by PDMAEMA–PHB–PDMAEMA (CDZP NPs)

The synthesis of Dox: 50 mg of doxorubicin hydrochloride was dissolved in 4 mL of methanol, and 40 μL of triethylamine was added to the system and evenly mixed. The mixed system was added dropwise to 20 mL of deionized water while being stirred and the stirring was continued for 24 h. After the reaction, the mixed system was centrifuged to obtain precipitation, which was washed with deionized water three times, and then freeze-dried.

The synthesis of CD: 1 mg of Dox was dissolved in 1 mL of DMF, and 35.9 mg of $Cu(CO_2CH_3)_2{\cdot}H_2O$ was dissolved in 1 mL of DMF. 5 μL of the above solution was mixed with Dox solution and stirred for 30 min. After the reaction, the mixed system was centrifuged and the precipitation was washed twice with deionized water.

The synthesis of CDZ: CD obtained in the previous step was dissolved in 1 mL of DMF, and 2 mg of ZnPc was dissolved in 2 mL of DMF. Then, these solutions were mixed evenly and stirred for 4 h. After that, the mixed system was added dropwise to 7 mL of deionized water while being stirred and the stirring was continued for 30 min.

The synthesis of CDZP NPs: 200 μL of aqueous solution of PDMAEMA–PHB–PDMAEMA (0.5 mg mL^{-1}) was mixed with 4.8 mL of CDZ solution. Then the polymer was modified on the surface of CDZ with the help of an ultrasonic homogenizer (JY92-II DN). The concentration of CDZP NPs was written as the concentration of Dox contained without special instructions.

Characterization of the nanoparticles

Transmission electron microscopy (TEM) (G2 Spirit Biotwin, USA) was used to observe the morphology of CDZP NPs. Dynamic light scattering (DLS) (Zetasizer Nano ZS-90, UK) was used to determine the size and stability of CDZ and CDZP NPs.

X-ray photoelectron spectroscopy (XPS) (PANalytical X'Pert PRO, Netherlands), energy dispersive spectroscopy (EDS) (SUPRA55 SAPPHIRE, Germany), a fluorescence spectrophotometer (Cary Eclipse EL07114196, USA), Fourier transform infrared (FT-IR) spectrum (Avatar370, USA) and UV-vis-NIR spectrophotometer (UV-1750, Japan) were used to determine the properties of the samples. A multi-mark detection system (Victor3V, USA), UV-vis-NIR spectrophotometer (UV-1750, Japan), and inductively coupled plasma-optical emission spectrometry (SPECTRO SPECTROBLUE FMX36, Germany) were used to determine the encapsulation efficiency and drug loading of CDZP NPs.

In vitro drug release

Firstly, the fluorescence spectrum of CD in the presence of GSH was studied to investigate its GSH responsiveness.

In addition, CDZP NPs with or without 638 nm laser irradiation (1 W cm^{-2}, 10 min) were placed in the dialysis bag, and then placed in phosphate buffer of different pH (6.5 or 7.4). A certain amount of release medium was taken out at 0, 1, 2, 4, 6, 8, 10, 12, 24, 36, 48, 60, 72, 84, and 96 h respectively, and the same amount of release medium of the same type was supplemented. Among them, GSH was added to the dissolution medium, and the final concentration was 10 mM. The release behavior of CDZP NPs was studied by detecting Dox concentration using a Multi-mark detection system (Victor3V, USA).

In vivo photothermal effect

Explore the photothermal effects of different systems, laser power, and CDZP NP concentrations under 638 nm laser irradiation. The photothermal stability test was conducted using a laser irradiation-cooling cycle of 6 rounds. Use a thermocouple thermometer (TES-1310, China) to record temperature changes every 30 seconds.

Production of extracellular singlet oxygen ($^1O_2$)

ABDA was mixed with different combinations of drugs (ZnPc, CDZP NPs, CDZP NPs + GSH), irradiated with a 638 nm laser (1 W cm^{-2}) for different times (0, 0.5, 1, 2, 3, 4, 5, 6, 8, 10, 15 and 20 min), and detected using a UV-vis-NIR spectrophotometer (UV-1750, Japan). Among them, the final concentrations of ABDA and GSH are 50 μg mL^{-1} and 2 mM respectively, and the final concentrations of ZnPc contained in free ZnPc and CDZP NPs are 50 μg mL^{-1}. The capture agent DMPO (100 mM, 50 μL) was incubated with H_2O, ZnPc (+ laser), CDZP (+ laser) for 2 min, and detected using an electron paramagnetic resonance (EPR) spectrometer (EMXplus-9.5/12, USA).

Extracellular GSH depletion

Explore the GSH consumption behavior of systems with different drug combinations, GSH concentrations, and CDZP NP concentrations. After sampling, mix with five times the volume of DTNB analytical solution (0.1 mM). The samples were incubated at room temperature for 10 min and tested using a UV-vis-NIR spectrophotometer (UV-1750, Japan).

Production of extracellular hydroxyl radical ($^{\bullet}OH$)

CDZP NPs with different concentrations were mixed with GSH, H_2O_2, and TMB, incubated at 37 °C for 6 h and 12 h, and detected using a UV-vis-NIR spectrophotometer (UV-1750, Japan). The final concentrations of GSH, H_2O_2, and TMB were 1 mM, 1 mM, and 0.2 mM, respectively. The final concentrations of CDZP NPs were 6.25, 12.5 and 25 μg mL^{-1}.

GSH was mixed with H_2O_2, D/Z/P + H_2O_2, and CDZP NPs + H_2O_2 respectively, and the final concentrations of GSH and H_2O_2 were 1 mM. After mixing evenly, the above system (50 μL) was mixed with the capture agent DMPO (100 mM, 50 μL), incubated for 2 min, and detected using an electron paramagnetic resonance (EPR) spectrometer (EMXplus-9.5/12, USA).

Cellular uptake

HeLa cells were inoculated and cultured in a 12 well plate for 24 h. The original medium was replaced with serum-free medium containing a physical mixture of C/D/Z or CDZP NPs

(5 μg mL^{-1}), and continued to be cultured for 1 or 4 h. After treatment, the cells were washed three times with PBS and collected, and analyzed with FC (ATTUNE NXT, USA). The cells were treated in the same way, the nuclei were stained with DAPI, and observed using a confocal laser scanning microscope (CLSM) (Zeiss LSM5, Germany).

Intracellular GSH depletion

HeLa cells were inoculated and cultured in a 12 well plate for 24 h. The original medium was replaced with serum-free medium containing CDZP NPs (2.5 μg mL^{-1}) and continued to be cultured. The cells were collected at different time points (0, 4 and 12 h) and determined by GSH detection kit.

Production of intracellular ROS

HeLa cells were inoculated and cultured in 12 well plates for 24 h. The original medium was replaced with serum-free medium containing free ZnPc, C/D/Z/P, or CDZP NPs, and continued to be cultured for 4 h. The concentrations of Dox and ZnPc were the same as those of CDZP NPs, and the concentration of Dox was 2.5 μg mL^{-1}. After treatment, the drug containing medium was replaced with serum-free medium containing DCFH-DA (10 μM), and incubation was continued for 30 min. After incubation, the cells were washed with serum-free medium 3 times, then irradiated with a 638 nm laser (1 W cm^{-2}, 2 min) and observed with a Leica fluorescence microscope (DM5500B, Germany). Similarly, 3-CCA and SOSG were added and incubated for 30 min to assess the intracellular $^{\bullet}OH$ and $^{1}O_2$ levels, respectively.

In vitro cytotoxicity

HeLa cells were inoculated in 96 well plates and cultured for 24 h. The original medium was replaced with serum-free medium containing C/D/Z/P or CDZP NPs, and continued to be cultured for 20 h with or without 638 nm laser irradiation (1 W cm^{-2}, 2 min). The concentrations of Cu^{2+}, Dox and ZnPc contained in C/D/Z/P were the same as those of CDZP NPs, and the concentrations of Dox were 0.625, 1.25, 2.5, 5, 10 and 20 μg mL^{-1} respectively. After treatment, the drug containing medium was replaced with MTT solution (0.5 mg mL^{-1}) and continued to incubate for 4 h. After incubation, the MTT solution was removed, then DMSO was added. The mixed system was detected using a Microplate reader (Bio T ek ELX800, USA).

Live/dead cell staining

HeLa cells were inoculated and cultured in a 12 well plate for 24 h. The original medium was replaced with serum-free medium containing CDZP NPs (2.5 μg mL^{-1}), and continued to be cultured for 6 h. Subsequently, remove the original culture medium and add serum-free culture medium without drugs for another 4 h with or without 638 nm laser irradiation (1 W cm^{-2}, 2 min). Calcein-AM/PI live/dead cell double staining kit was used for detection and a Leica fluorescence microscope (DM5500B, Germany) was used for analysis.

Apoptosis

HeLa cells were inoculated and cultured in a 12 well plate for 24 h. The original medium was replaced with serum-free medium containing C/D/Z/P or CDZP NPs (2.5 μg mL^{-1}), and continued to be cultured for 20 h with or without 638 nm laser irradiation (1 W cm^{-2}, 2 min). Annexin V-FITC/PI apoptosis detection kit was used for detection and flow cytometry (FC) (ATTUNE NXT, USA) was used for analysis.

Hemolysis experiment

Freshly collected mouse periocular venous blood was centrifuged (10 000 rpm, 10 min, 4 °C) and washed three times with cold PBS. The precipitated blood cells were diluted to 10% (V/V_0) with PBS. CDZP NPs were added to diluted blood cells at 37 °C and incubated for 2 h. The negative control group selected PBS, while the positive control group selected deionized water. The final concentrations of CDZP NPs were 1.5625, 3.125, 6.25, 12.5, 25 and 50 μg mL^{-1} respectively. After incubation, the mixed system was centrifuged (10 000 rpm, 10 min, 4 °C) and the supernatant was observed. Measure the absorbance of each group of supernatant at 560 nm using a Microplate reader (Bio T ek ELX800, USA), and the hemolysis rate is calculated as:

$$\text{Hemolysis rate } (\%) = \frac{\text{Experimental group absorbance} - \text{Negative control group absorbance}}{\text{Positive control group absorbance} - \text{Negative control group absorbance}} \times 100\%$$

In vitro fluorescence imaging

Dissolve CDZP NPs in DMF and sonicate for 30 min to prepare depolymerized CDZP NPs (25, 12.5, 6.25, 3.125, 1.5625 μg mL^{-1}). In addition, CDZP NPs were dissolved in water and prepared into the same concentration gradient to prepare nanoparticles in an undissolved state. Finally, the *in vitro* fluorescence imaging effect of CDZP NPs before and after depolymerization was detected using an imaging system (IVIS Lumina II, USA).

In vivo fluorescence imaging

PBS or CDZP NPs were injected into tumor bearing nude mice by tail vein injection. The content of ZnPc in CDZP NPs was 2 mg kg^{-1}. The imaging system (IVIS Lumina II, USA) was used for detection at 4, 8, 12, 24 and 48 h respectively. After the experiment, the mice were killed, and the main organs and tumors were dissected and detected using the imaging system (IVIS Lumina II, USA).

In vivo photothermal effect

PBS or CDZP NPs were injected into tumor bearing nude mice by tail vein injection. The content of ZnPc in CDZP NPs was

2 mg kg^{-1}. After 24 hours of drug administration, the drug was concentrated at the tumor site, and the temperature change of the tumor site under laser irradiation (638 nm, 1 W cm^{-2}, 3 min) and the overall thermal imaging of the mice were continuously detected with an infrared thermographic camera (Ax5, China).

In vivo anti-tumor effect and histopathologic analysis

The tumor-bearing mice were randomly divided into six groups with three mice in each group. The corresponding drugs were injected on the 1st, 4th, 7th and 10th days respectively: (1) the negative control group was injected with 0.9% NaCl solution (200 μL), (2) the laser group (638 nm, 1 W cm^{-2}, 2 min, the same below), (3) physical mixture Cu^{2+}/Dox/ZnPc/PDMAEMA–PHB–PDMAEMA (C/D/Z/P) group, (4) C/D/Z/P combined with laser group, (5) CDZP NP group, and (6) CDZP NPs combined with laser group. The dosage of dox in C/D/Z/P and CDZP NPs was 1 mg kg^{-1}. During the treatment process (14 days), the weight of mice was recorded every day. The tumor size was measured with vernier caliper on the 1st, 3rd, 5th, 7th, 9th, 11th and 13th days to calculate the tumor volume. The tumor volume is calculated as:

$$V = \frac{(\text{tumor length}) \times (\text{tumor width})^2}{2}$$

The relative tumor volume is V/V_0, and V_0 is the initial volume of the tumor before treatment. After the experiment, the mice were killed and dissected to obtain their main organs and tumors for H&E staining analysis.

Statistical analysis

Statistical significance was calculated by Student's *t*-test. *P* value <0.01 was considered to be statistically significant (***: $p < 0.01$, **: $p < 0.05$).

Results and discussion

Synthesis and characterization of CDZP NPs

The synthesis process of CDZP nanoparticles (NPs) was shown in Fig. 1(A). After intravenous injection, CDZP NPs accumulated at the tumor site and depleted GSH for enhanced synergistic therapy (Fig. 1(B)).

As shown in Fig. 2(A), CDZP NPs were uniformly dispersed with spherical morphology. And the dynamic light scattering (DLS) analysis demonstrated similar results in Fig. 2(B). The hydration diameter of CDZP NPs was around 145 nm and the polydispersity index (PDI) was about 0.3. PDMAEMA–PHB–PDMAEMA, as amphiphilic copolymers with two hydrophilic (DMAEMA) blocks (Fig. S1–S3 and Table S1, ESI†), could be attached to the unstable core of CDZ NPs through hydrophobic force, and the tertiary amine group of the hydrophilic part of the polymer could enhance the hydrophilicity and stability of CDZP NPs. Compared with CDZ, surface modification with a small amount of PDMAEMA–PHB–PDMAEMA (P) polymer resulted in a significant decrease in the particle size and PDI of the obtained CDZP NPs, indicating that surface modification with a small amount of polymer can further reduce particle size and improve the uniformity of nanoparticles. The element

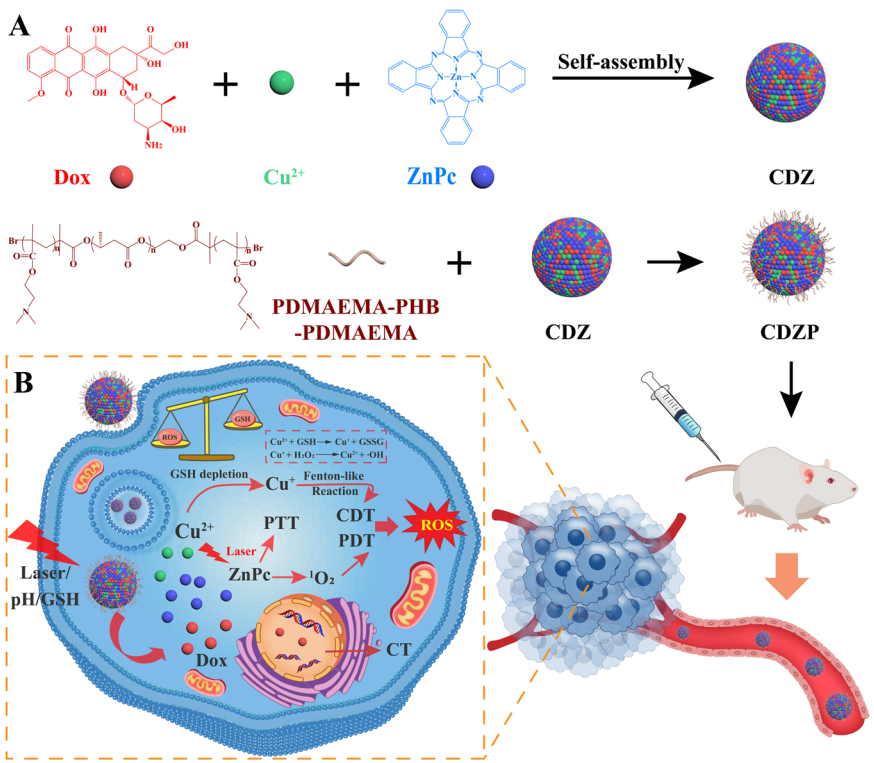

Fig. 1 (A) Synthesis process and (B) tumor microenvironment (TME) modulation enhanced therapeutic mechanism of CDZP nanoparticles *in vivo*.

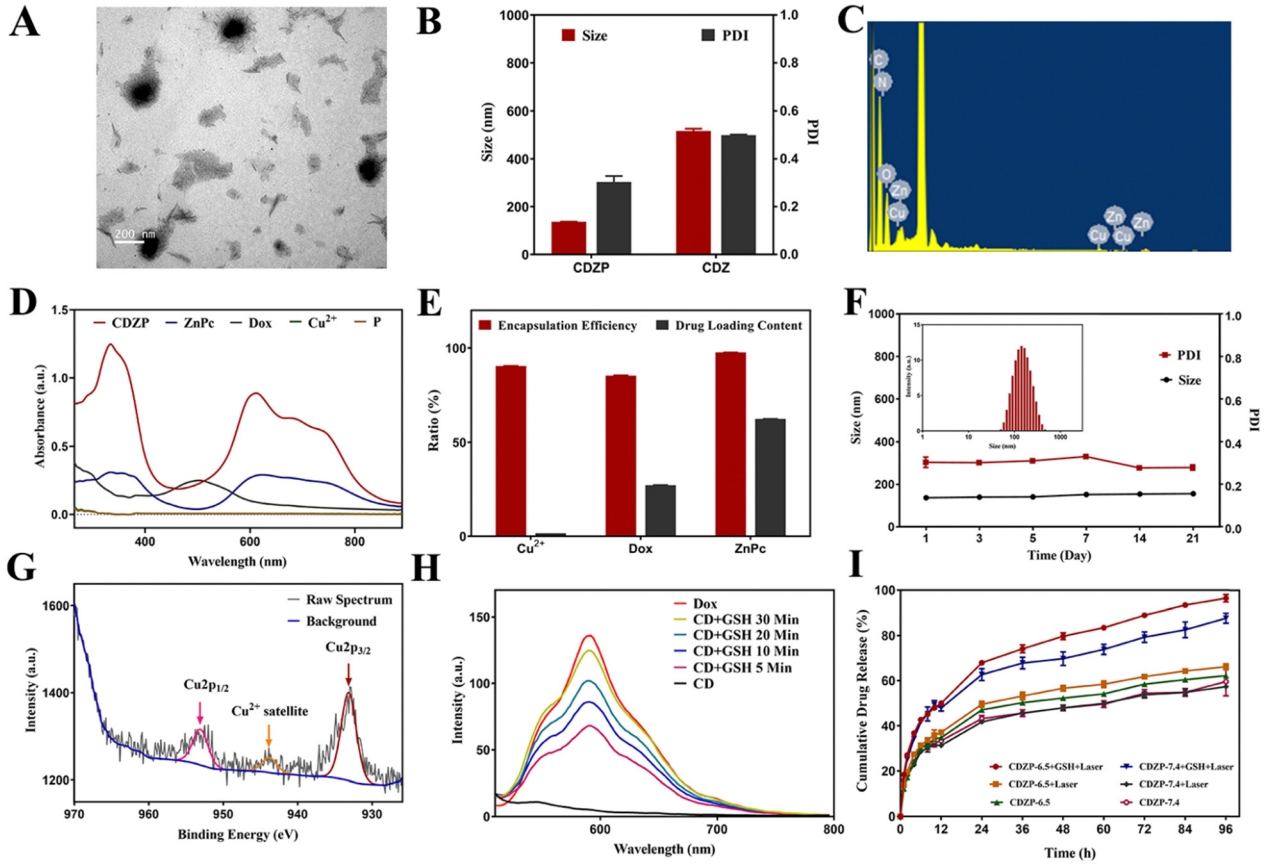

Fig. 2 Characterization of CD and CDZP NPs. (A) Transmission electron microscopy (TEM) image of CDZP NPs (scale bar = 200 nm). (B) Particle size and PDI of CDZ and CDZP NPs (n = 3). (C) EDS analysis of CDZP NPs. (D) UV-vis-NIR spectrum of Cu^{2+}, Dox, ZnPc, P and CDZP NPs. (E) Encapsulation efficiency and drug loading content of Cu^{2+}, Dox, and ZnPc in CDZP NPs (n = 3). (F) Change of particle size and PDI of CDZP NPs in 21 days (n = 3). (G) XPS spectrum of Cu 2p in CD. (H) Fluorescence emission spectra of Dox, CD, CD + GSH at different incubation times. (I) Cumulative release of Dox from CDZP NPs under different conditions (n = 3).

distribution of CDZP NPs was studied by energy dispersive spectroscopy (EDS). In Fig. 2(C), the distinct distribution of copper and zinc elements, served as evidence of the successful loading of each component within the NPs.

In the Fourier transform infrared (FTIR) spectrum (Fig. S4, ESI†), a special signal peak of polymer P at 2800–3000 cm^{-1} was observed in CDZP NPs. At the same time, the physical mixture of C/D/Z/P exhibited characteristic signal peaks around 3300–3400 cm^{-1}, 1500 cm^{-1}, and 1650–1900 cm^{-1}, corresponding to the stretching vibration peak of the phenolic hydroxyl group of Dox, the dense signal peak of ZnPc, and the carbonyl peak of polymer P. However, the three signal peaks mentioned above were not observed in CDZP NPs. The results confirmed that CDZP NPs were not the physical mixtures of several raw drugs, instead, they were interconnected by π–π stacking, coordination effect and hydrophobic force.

In addition, as displayed in Fig. 2(D), the UV-vis spectrum further substantiated the successful synthesis of CDZP NPs. Notably, the absorption peak of ZnPc in CDZP NPs increased significantly, indicating that loading of ZnPc into CDZP NPs can significantly improve the light absorption ability, which was expected to enhance the PDT and PTT effects. As shown in the Fig. 2(E), CDZP NPs were synthesized through self-assembly without the involvement of drug carriers. Consequently, the CDZP NPs had a high encapsulation and drug loading efficiency, thus facilitating their effective triple anti-tumor effects.

The size and PDI of CDZP NPs had no significant change within 21 days, indicating that the CDZP NPs have excellent stability (Fig. 2(F)). However, the particle size of CDZ increased from 500 nm to 1500 nm within 21 days while PDI increased from 0.5 to 1 (Fig. S5, ESI†) indicating the poor particle stability. The above results suggested that the surface modification with a small amount of polymer P was essential for reducing the particle size and improving the stability and uniformity. In addition, the CDZP NPs showed good colloidal stability in DMEM with 10% FBS for 24 h (Fig. S6, ESI†), having great potential for further *in vivo* studies.

Cu^{2+} can undergo redox with GSH, so as to consume the overexpression of GSH in TME, while other valence copper cannot complete this process. As shown in Fig. S7 (ESI†), there were peaks of C 1s, N 1s, O 1s and Cu 2p in the X-ray photoelectron spectroscopy (XPS) spectrum of Cu-Dox (CD). The spectrum of Cu 2p in CD (Fig. 2(G)) further showed Cu $2p_{1/2}$, Cu $2p_{3/2}$ and Cu^{2+} satellite peaks, indicating that copper

in CD exists in the form of Cu^{2+} and can be used for GSH consumption.

For the responsive release behavior of drug stimulation, a preliminary study was conducted on the GSH responsiveness of CD by measuring the fluorescence emission spectra under different conditions (Fig. 2(H)). Following the formation of CD, Dox fluorescence was found to undergo quenching. Subsequently, GSH was introduced to the CD system. As the incubation time was extended, the fluorescence of Dox gradually recovered, suggesting that GSH is capable of disrupting the chelation between CDs, and facilitating the gradual release of Dox. In addition, through the measurement of the release behavior of CDZP NPs, it could be seen that in addition to GSH responsiveness, CDZP NPs also exhibited sensitivity toward pH and laser stimulation. Their responsiveness came from the acid sensitivity and thermal sensitivity of polymer P. This triple-stimulus-responsive drug release manner had the potential to reduce the toxicity of CDZP NPs toward normal cells and further improved the inhibitory efficiency on tumor sites.

Evaluation of photothermal effect *in vitro*

To study the *in vitro* photothermal effect of CDZP NPs, the temperature changes of different systems under laser irradiation were recorded. As shown in Fig. 3(A), after the end of laser irradiation, the temperature of the deionized water increased by 14.2 °C, the temperature of the free ZnPc increased by 17.3 °C, and the temperature of the CDZP NPs increased by 25.5 °C, indicating that compared with free ZnPc, CDZP NPs have a better *in vitro* photothermal conversion performance. This phenomenon can be attributed to the formation of supramolecular assembly through π–π stacking by ZnPc, leading to the suppression of its fluorescence emission. This alteration facilitated the conversion of energy to heat energy. Finally, stronger photothermal conversion efficiency was obtained, which was conducive to giving full play to the photothermal effect to kill tumor cells. In addition, as the concentration of CDZP NPs and laser power increase, the system temperature increased more after irradiation. This revealed that the photothermal effect of CDZP NPs *in vitro* had a significant concentration dependence and irradiation laser power dependence (Fig. 3(B) and (C)). Further research was conducted on the photothermal stability of the two groups by using a laser irradiation natural cooling six cycle method. As shown in Fig. 3(D), with the increase of the number of cycles, the maximum temperature that could be reached by free ZnPc slightly decreased, while CDZP NPs could reach the highest temperature during the first heating within six cycles, and the photothermal conversion effect remained unchanged. This revealed that CDZP NPs had good photothermal stability. Afterwards, by selecting the temperature change data of the cooling process of CDZP NPs after the first laser irradiation in the stability experiment and fitting it (Fig. 3(E) and (F)), the photothermal conversion efficiency of CDZP NPs could be calculated to be 49.88%.

Evaluation of the photodynamic, chemodynamic and GSH depletion effect *in vitro*

The *in vitro* photodynamic performance of CDZP NPs was tested using 9,10-anthracenediyl-bis(methylene)dimalonic acid (ABDA) as the $^1O_2$ indicator. As shown in Fig. 4(A) and (B), under laser irradiation, the absorption value of ABDA co-incubated with ZnPc slightly decreased, while the CDZP NP group showed a significant decrease. The ESR spectra showed that CDZP NPs had a little higher $^1O_2$ signal peaks under laser irradiation (Fig. S8, ESI†). This indicated that CDZP NPs had a better ability to induce $^1O_2$ production, which was conducive to

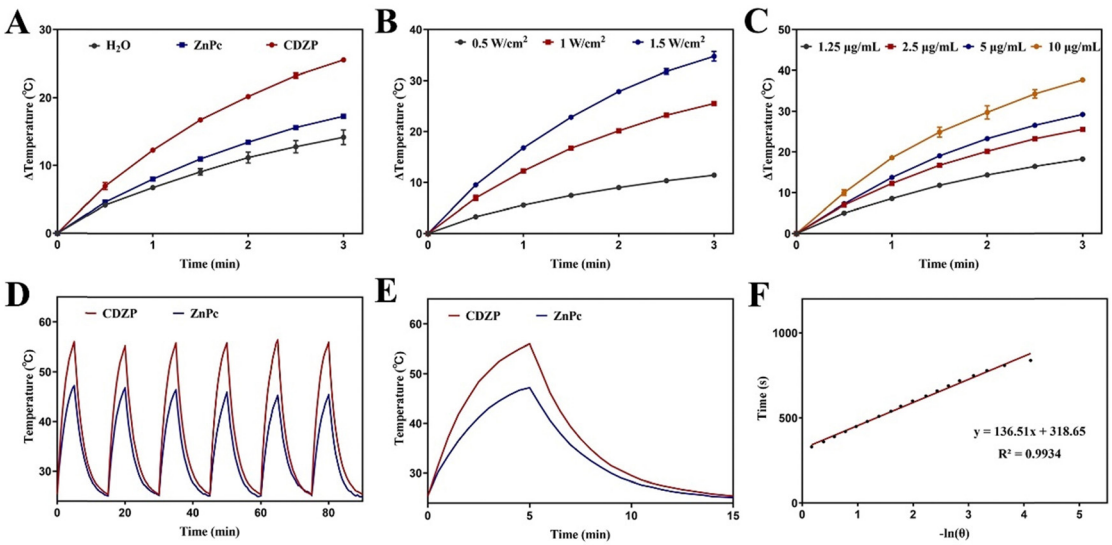

Fig. 3 Photothermal effect *in vitro*. (A) Temperature changes of different systems under laser irradiation (n = 3). (B) Temperature changes of CDZP NPs under different power laser irradiation (n = 3). (C) Temperature changes of CDZP NPs with different concentrations under laser irradiation (n = 3). (D) Temperature changes of free ZnPc and CDZP NPs during six cycles. (E) Temperature changes of free ZnPc and CDZP NPs during the first laser irradiation and natural cooling process. (F) Time–(−ln(θ)) fitting line of CDZP NPs.

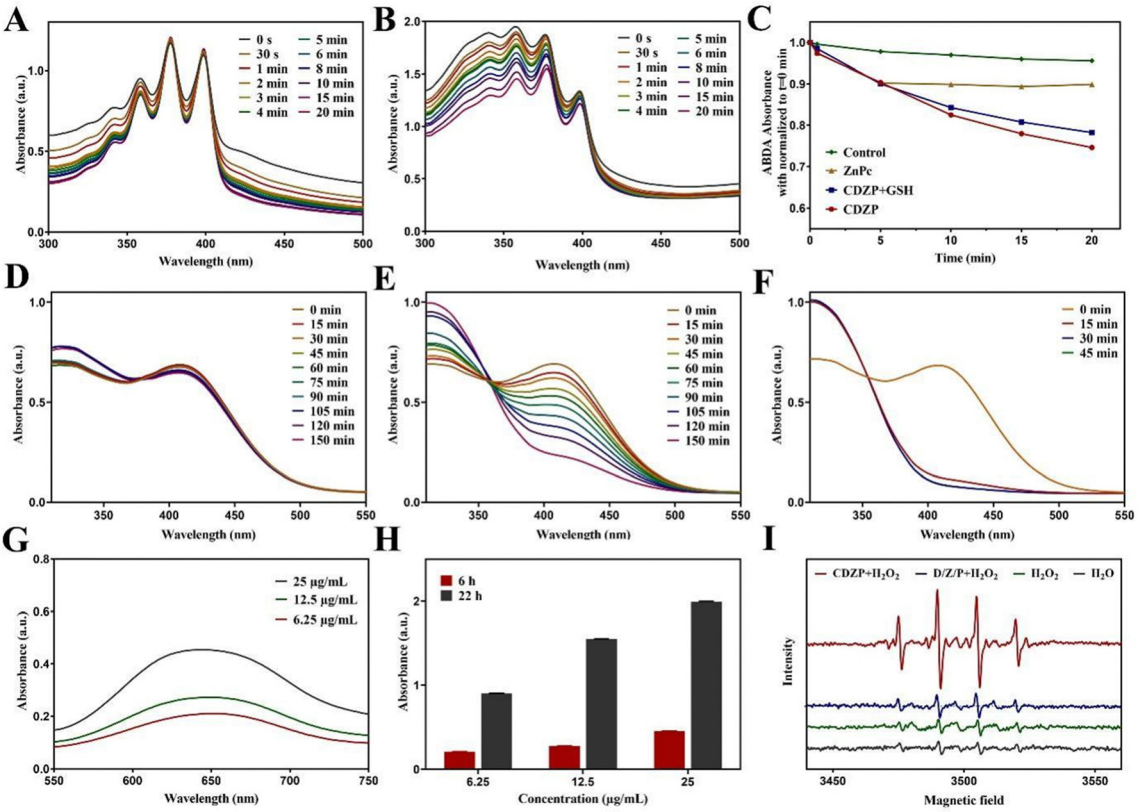

Fig. 4 Photodynamic, chemodynamic and GSH depletion effect *in vitro*. UV-vis spectrum of ABDA co-incubated with (A) free ZnPc and (B) CDZP NPs. (C) ABDA absorbance normalized to t = 0 min of different groups at different laser irradiation times. UV-vis spectrum of DTNB co-incubated with (D) D/Z/P + GSH, (E) CDZP + GSH, and (F) CDZP + GSH + laser at different times. (G) Vis spectrum of TMB co-incubated with GSH, H_2O_2, and CDZP NPs at different concentrations for 6 h. (H) TMB absorbance co-incubated with GSH, H_2O_2, and CDZP NPs at different concentrations for 6 and 22 h (n = 3). (I) Detection signals of the EPR spectrometer in different systems.

its better *in vitro* photodynamic effects. Overexpression of GSH in tumors can clear ROS, seriously affecting the anti-tumor effect of ROS based treatment methods. CDZP NPs could dissociate Cu^{2+} to consume GSH and avoid GSH affecting the photodynamic effect. As shown in Fig. S9 (ESI†), a significant decrease in the absorption value of ABDA was also observed in the system with GSH, indicating that CDZP NPs have an excellent ability to produce photoinduced $^1O_2$ and could avoid the ROS-eliminating effect of overexpressed GSH on PDT (Fig. 4(C)).

To further investigate the consumption performance of nanoparticles on GSH, 5,5′-dithio bis-(2-nitrobenzoic acid) (DTNB) was used as a detection agent for specific research. The absorbance of the control group (Fig. S10, ESI†) and D/Z/P group (Fig. 4(D)) showed almost no change, while the absorbance of the CDZP NP group showed a significant decrease, exhibiting time-dependent GSH consumption behavior (Fig. 4(E)). This was because Cu^{2+} released from CDZP NPs could undergo redox with GSH, consume GSH, and thus enhance the ROS based oxidative stress killing effect. At the same time, Cu^{2+} could be reduced to Cu^{+}, providing a prerequisite for catalyzing a Fenton-like reaction and playing the role of CDT. By applying laser irradiation to the system, as shown in Fig. 4(F), the GSH in the system was almost completely consumed at 15 minutes, which was consistent with the results of *in vitro* photodynamic experiments. This once again demonstrated that CDZP NPs had good PDT effects. By changing the concentration of CDZP NPs and GSH in the mixed system, it could be seen that the GSH consumption behavior of nanoparticles had a significant concentration dependence and good consumption ability (Fig. S11 and S12, ESI†).

Besides, the ROS-generated ability of NPs was studied using 3,3′,5,5′-tetramethylbenzidine (TMB) which could be oxidized by active $^{\bullet}OH$ and its absorption value at 650 nm increased. As displayed in Fig. 4(G) and (H), the vis absorption spectrum was detected after incubating TMB with CDZP NPs, revealing that CDZP NPs could generate $^{\bullet}OH$ in a concentration and time dependent manner. In addition, an electron paramagnetic resonance (EPR) spectrometer further confirmed an identical result (Fig. 4(I)) that in the presence of GSH and H_2O_2, the produced Cu^{+} could generate $^{\bullet}OH$ through a Fenton-like reaction. The above results demonstrated that CDZP NPs had the potential for CDT.

Evaluation of cellular uptake, intracellular GSH depletion and the ROS generation effect

The cellular uptake behavior in HeLa cells was studied using a confocal laser scanning microscope (CLSM) and flow cytometry (FC). HeLa cells were incubated with C/D/Z and CDZP NPs for

1 h and 4 h. As shown in Fig. 5(A), the cellular uptake behavior of C/D/Z and CDZP NPs was time-dependent, and the fluorescence intensity of CDZP NPs was significantly stronger than that of C/D/Z with identical incubation times. The successful synthesis of CDZP NPs improved the drug solubility and enhanced the cellular uptake of active substance by endocytosis. The results of FC further confirmed that CDZP NPs could be taken up by cells in a larger amount than C/D/Z, as evidenced by the increased fluorescence of Dox. Additionally, the uptake exhibited a time-dependent pattern (Fig. 5(B) and (C)).

The GSH consumption behavior of CDZP NPs in HeLa cells was studied using the DTNB thiol detection kit. As shown in Fig. 5(D), the content of GSH in cells gradually decreased with the prolongation of incubation time. This result confirmed that CDZP NPs could deplete GSH with a time-dependent manner in HeLa cells and was expected to enhance the ROS-based therapy.

2,7-Dichlorodihydrofluorescein diacetate (DCFH-DA) was used as a probe to detect the production of ROS generated by CDZP NPs in HeLa cells. DCFH-DA could transform into 2,7-dichlorofluorescein (DCF) and emit fluorescence after reacting with ROS. As shown in Fig. 5(E), no significant green fluorescence was observed in the control, laser, and ZnPc group. The C/D/Z/P group had weak fluorescence. Combined with the results of the *in vitro* GSH depletion experiment, it could be seen that this was because free Cu^{2+} and intracellular over-expressed GSH undergo redox, generating Cu^{+} to trigger CDT, thus producing ROS. The CDZP NP group had stronger signals than C/D/Z/P, which was due to its higher cell uptake efficiency. As shown in Fig. S13 (ESI†), intracellular •OH was determined

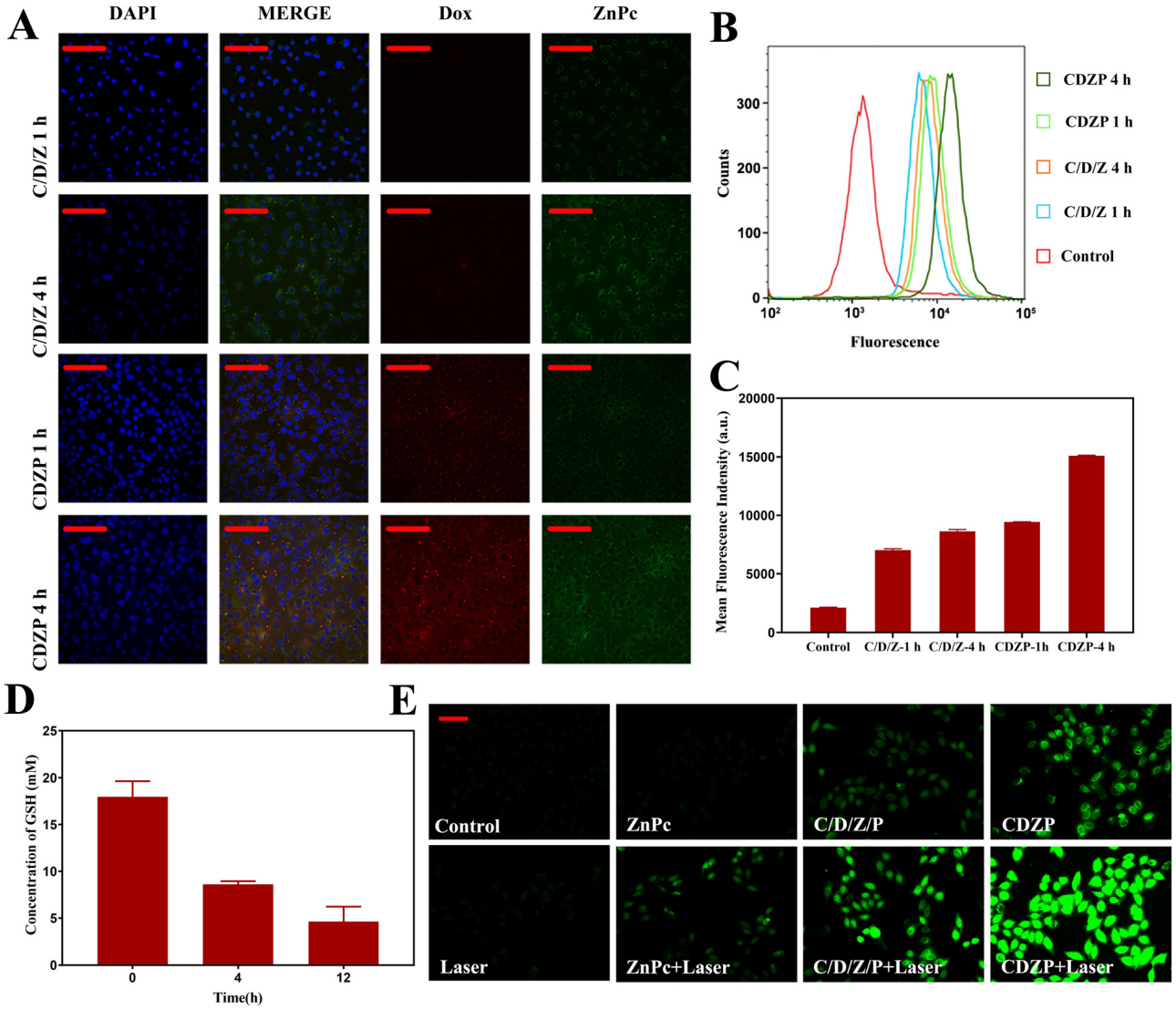

Fig. 5 Cellular uptake, intracellular GSH depletion and ROS generation. (A) CLSM images of HeLa cells co-incubated with C/D/Z and CDZP NPs for 1 h and 4 h (scale bar: 100 μm). (B) FC results and (C) average fluorescence intensity of HeLa cells co-incubated with C/D/Z and CDZP NPs for 1 h and 4 h (n = 3). (D) GSH levels in HeLa cells after co-incubation with CDZP NPs for different times (n = 3). (E) Fluorescence signals of DCF in HeLa cells under different treatment conditions (scale bar: 100 μm).

by coumarin-3-carboxylic acid (3-CCA). CDZP-treated cells demonstrated obviously significant green fluorescence, suggesting the considerable potential of •OH generation for CDT. The laser irradiation group observed stronger green fluorescence signals than the non-laser group. This phenomenon can be attributed to the properties of ZnPc, which could generate $^1O_2$ under laser irradiation (Fig. S14, ESI†). The coalescence of CDZP NPs and laser irradiation showed the strongest green fluorescence, providing evidence that NPs can reduce ROS clearance by depleting GSH. As a result, this combination more effectively enhanced the effects of CDT and PDT.

Evaluation of cytotoxicity

In order to study the cytotoxicity of CDZP NPs, different drugs were incubated with HeLa cells to study the cell survival rate using the standard methyl thiazolyl tetrazolium (MTT) assay. CDZP NPs displayed negligible cytotoxicity toward L929 which is a kind of normal cell, even at a high concentration of 20 μg mL^{-1} (Fig. S15, ESI†). Fig. 6(A) suggested that the toxicity of drugs on HeLa cells was concentration dependent. With the increase of drug concentration, the cell survival rate decreased and the toxicity was enhanced. In the absence of laser irradiation, both C/D/Z/P and CDZP NPs had a certain degree of cytotoxicity, which was due to their therapeutic effects of chemotherapy and CDT. The higher cell uptake efficiency resulted in CDZP NPs exhibiting lower cell survival rates and stronger cytotoxicity compared to C/D/Z/P. The combination of CDZP NPs and laser irradiation showed the strongest cytotoxicity. In addition, laser irradiation could accelerate the release of active drugs. Simultaneously, ZnPc could generate $^1O_2$ and release heat, achieving PDT and PTT, effectively exerting the triple synergistic therapeutic effect of chemotherapy, phototherapy, and CDT.

In the live/dead cell staining experiment, the CDZP NPs combined with laser irradiation group showed the strongest red fluorescence of dead cells (Fig. 6(B)). In the cell apoptosis experiment, this group had the highest cell apoptosis rate (Fig. 6(C)). These two results were consistent with the MTT results, reconfirming that CDZP NPs under laser irradiation were capable of depleting GSH and effectively enhancing triple anti-tumor effects.

Evaluation of anti-tumor *in vivo*

Before conducting *in vivo* experiments, the biological safety of CDZP NPs was evaluated through hemolysis experiments. As shown in Fig. 7(A), the optical images of the supernatant treated with CDZP NPs resembled those of the negative control, and no significant hemolytic effect was observed. By measuring the absorbance of the supernatant, it was calculated that the hemolysis rate was below 5%, indicating that CDZP NPs have good biocompatibility and can be used for subsequent *in vivo* efficacy evaluation experiments (Fig. S16, ESI†).

The depolymerized CDZP NPs exhibited concentration dependent fluorescence imaging effects *in vitro* (Fig. S17, ESI†). Given the aforementioned fluorescence spectrum, ZnPc and CDZP NPs were utilized as contrast agents to study the

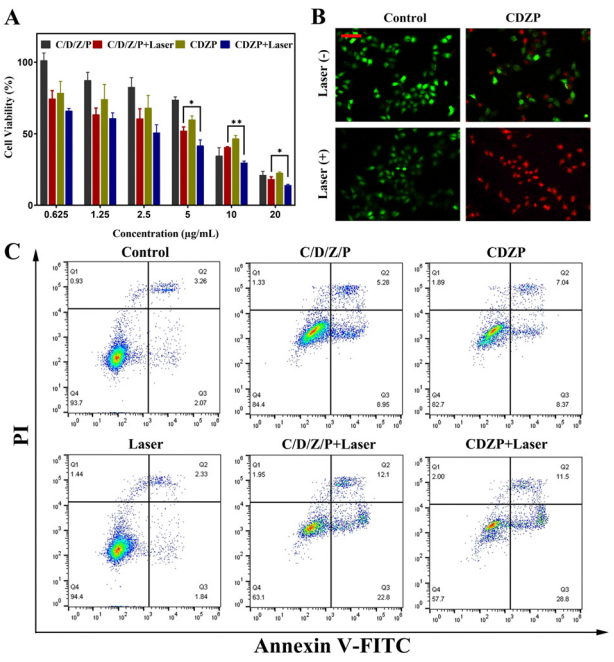

Fig. 6 Cytotoxicity. (A) Cell viability of HeLa cells under different treatment conditions (n = 6, $^{**}p < 0.01$, $^{*}p < 0.05$). (B) Live/dead cell staining results of HeLa cells under different treatment conditions (scale bar = 100 μm). (C) FC analysis of HeLa cell apoptosis under different conditions.

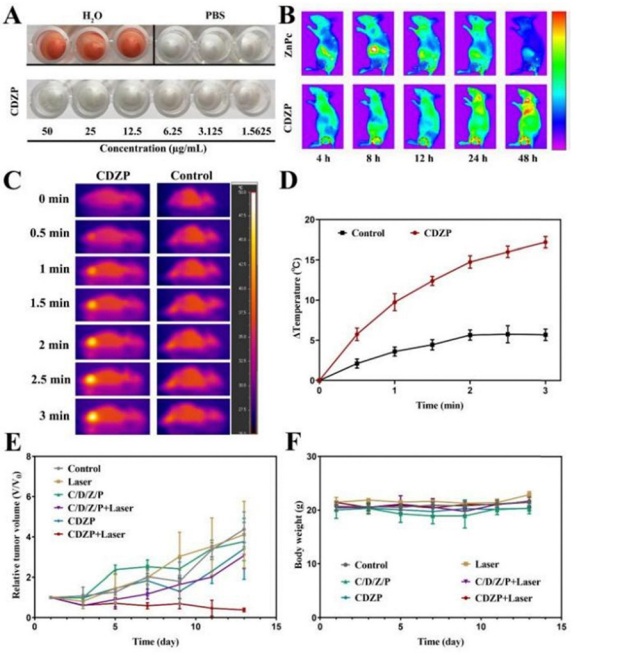

Fig. 7 Hemolysis, *in vivo* fluorescence, photothermal and anti-tumor analysis. (A) Optical images of the hemolysis evaluation of CDZP NPs at different concentrations. (B) Fluorescence images at different time points after intravenous injection of free ZnPc and CDZP NPs. (C) Infrared thermal imaging and (D) temperature changes after intravenous injection of CDZP NPs at different time points (n = 3). (E) Tumor growth curve and (F) body weight curve of different groups of mice during treatment (n = 3).

biodistribution condition *in vivo*. Compared to ZnPc, CDZP NPs could specifically accumulate at the tumor site due to the EPR effect (Fig. S18, ESI†) and the fluorescence intensity increased with the extension of time within 48 h (Fig. 7(B)), enhancing the effectiveness of tumor treatment.

The *in vivo* photothermal effect of CDZP NPs was studied using infrared imaging technology. The infrared thermal imaging of the PBS group showed only slight changes (Fig. 7(C)). Subsequent temperature measurements at the tumor site revealed following 3 min of irradiation, the temperature at the tumor site was 38.9 °C. The temperature of the tumor site in mice injected with CDZP NPs continued to rise, reaching a maximum temperature of 49.7 °C (Fig. 7(D)). Research has confirmed that tumor cells can undergo cell death at a temperature of 42 °C, indicating that CDZP NPs have good *in vivo* photothermal effects and can effectively damage tumor cells through the photothermal pathway, exerting therapeutic effects.

Inspired by the above satisfying results, the *in vivo* antitumor effect of CDZP NPs was evaluated. As shown in Fig. 7(E), the tumor volume of mice in the negative control group and laser group increased rapidly. The C/D/Z/P group, CDZP NPs group, and the C/D/Z/P combined laser group had a certain inhibitory effect on tumor growth, and the inhibitory effect gradually improved. This was because the C/D/Z/P group and the CDZP NP group could only play the role of chemotherapy and CDT. Due to the superior targeted accumulation of CDZP NPs at the tumor site compared with the physical mixture through the EPR effect, the therapeutic effect has been improved. The C/D/Z/P combined laser group can play a combined role of chemical, phototherapy and chemodynamic treatment, and its tumor inhibition effect was further improved. The combination of CDZP NPs and laser irradiation had the strongest tumor therapeutic effect, indicating that CDZP NPs can exert their dual advantages of tumor targeting and triple anti-tumor, effectively inhibiting tumor growth.

During the treatment, there was no significant change in the weight of mice between groups, indicating that the nanoparticles had good safety and were not toxic to mice (Fig. 7(F)). After the experiment, the main organs of the mice were stained with H&E for histopathological analysis. As displayed in Fig. S19 (ESI†), the CDZP NP group had no damage to the main organs, which further explained its safety. For tumor tissue, it could be seen that CDZP NPs combined with the laser group had the greatest tissue damage and the best therapeutic effect. In conclusion, CDZP NPs could regulate the redox level of tumor sites by consuming GSH, and enhance the synergistic effect of chemotherapy/phototherapy/chemodynamic therapy, which has a good application prospect.

Conclusions

A novel multifunctional CDZP nanosystem was developed *via* a green and straightforward self-assembled process. The nanoparticles accumulated at the tumor site and effectively responded to both laser irradiation and TME, leading to the controlled release of active substances. Notably, the released Cu^{2+} contributed to TME remodeling by depleting intracellular GSH and triggering a Fenton-like reaction with H_2O_2, producing $^{\bullet}OH$ for CDT. Furthermore, the depletion of GSH reduced the ROS consumption, enhancing the efficiency of CDT and PDT-mediated treatment. The simultaneous delivery of Dox further enhanced the therapeutic effect by inducing cancer cell apoptosis through chemotherapy, resulting in a synergistic triple anti-tumor impact involving phototherapy and chemodynamic therapy. As the "all in one" nanoparticle, CDZP NPs exhibit remarkable TME modulation capabilities and the ability to track drug distribution, making them a promising candidate for highly efficient cancer therapy.

Author contributions

D. Y. C. and X. Z. proposed the research direction. D. Y. C. and X. Z. guided the project and supervised the research. J. L. Y. and C. L. synthesized the materials and conducted the characterizations, *in vivo* and *in vitro* anti-tumor therapy. J. Q. G., M. L., B. Y. C., B. W. and X. W. Z. assisted with the experiments. All authors have given approval to the final version of the manuscript.

Conflicts of interest

There are no conflicts to declare.

Acknowledgements

The National Natural Science Foundation of China [grant number 82273872, 21706221, 81772278], the Natural Science Foundation of Fujian Province [grant number 2018J05143] and the Fundamental Research Funds for the Central Universities [grant number 20720200048, 20720190077] supported this work.

References

1 F. Tian, F. Li, L. Ren, Q. Wang, C. Jiang, Y. Zhang, M. Li, X. Song and S. Zhang, *ACS Sens.*, 2022, **7**, 3611–3633.
2 S. Xi, Y.-G. Yang, J. Suo and T. Sun, *Front. Bioeng. Biotechnol.*, 2022, **10**, 873369.
3 R. L. Siegel, K. D. Miller, N. S. Wagle and A. Jemal, *Ca-Cancer J. Clin.*, 2023, **73**, 17–48.
4 M. Zhang, X. Chen and N. Radacsi, *J. Controlled Release*, 2021, **329**, 96–120.
5 D. Wu, Y. Fan, H. Yan, D. Li, Z. Zhao, X. Chen, X. Yang and X. Liu, *Chem. Eng. J.*, 2021, **404**, 126481.
6 B. Ji, M. Wei and B. Yang, *Theranostics*, 2022, **12**, 434–458.
7 Q. Zeng, X. Ma, Y. Song, Q. Chen, Q. Jiao and L. Zhou, *Theranostics*, 2022, **12**, 817–841.
8 M. Zhan, F. Wang, Y. Liu, J. Zhou, W. Zhao, L. Lu, J. Li and X. He, *Adv. Sci.*, 2023, **10**, 2207200.
9 Z. Xiao, Q. Chen, Y. Yang, S. Tu, B. Wang, Y. Qiu, Y. Jiang, Q. Huang and K. Ai, *Chem. Eng. J.*, 2022, **449**, 137889.
10 Y. Yu, S. Wu, L. Zhang, S. Xu, C. Dai, S. Gan, G. Xie, G. Feng and B. Z. Tang, *Biomaterials*, 2022, **280**, 121255.

11 Q.-X. Wang, Y.-F. Yang, X.-F. Yang, Y. Pan, L.-D. Sun, W.-Y. Zhang, Y. Shao, J. Shen, J. Lin, L. Li and C.-H. Yan, *Nano Today*, 2022, **43**, 101439.
12 H. Guan, P. Zou, R. Lin, L. Xiao, Z. Fang, J. Chen, T. Lin, Y. Wang, Y. Peng, T. Zhong, B. Zhang, J. Lang, Y. Zhang, L. Xing, M. Chen and X. Xue, *Nano Energy*, 2023, **105**, 108002.
13 J. Zhu, C. Wang, Q. Wei, Y. Su, X. Qu, W. Wang, X. Song, X. Dong and Y. Cai, *Small*, 2023, **19**, 2303365.
14 S. L. Li, P. Jiang, F. L. Jiang and Y. Liu, *Adv. Funct. Mater.*, 2021, **31**, 2100243.
15 Z. Tang, Y. Liu, M. He and W. Bu, *Angew. Chem., Int. Ed.*, 2018, **58**, 946–956.
16 R. Niu, Y. Liu, Y. Wang and H. Zhang, *Chem. Commun.*, 2022, **58**, 7924–7927.
17 P. Manivasagan, A. Joe, H.-W. Han, T. Thambi, M. Selvaraj, K. Chidambaram, J. Kim and E.-S. Jang, *Mater. Today Bio*, 2022, **13**, 100197.
18 S. He, X. Jia, S. Feng and J. Hu, *Small*, 2023, **19**, 2300078.
19 Y. Huang, S. Wu, L. Zhang, Q. Deng, J. Ren and X. Qu, *ACS Nano*, 2022, **16**, 4228–4238.
20 Y. Liu, Y. Wang, X. Guan, Q. Wu, M. Zhang, P. Cui, C. Wang, X. Chen, X. Meng and T. Ma, *ACS Appl. Mater. Interfaces*, 2023, **15**, 26484–26495.
21 S. Koo, O. K. Park, J. Kim, S. I. Han, T. Y. Yoo, N. Lee, Y. G. Kim, H. Kim, C. Lim, J.-S. Bae, J. Yoo, D. Kim, S. H. Choi and T. Hyeon, *ACS Nano*, 2022, **16**, 2535–2545.
22 S. Fu, M. Wang, B. Li, X. Li, J. Cheng, H. Zhao, H. Zhang, A. Dong, W. Lu and X. Yang, *Biomater. Res.*, 2023, **27**, 43.
23 Y. Liu, R. Niu, R. Deng, S. Song, Y. Wang and H. Zhang, *J. Am. Chem. Soc.*, 2023, **145**, 8965–8978.
24 Z. Liu, S. Liu, B. Liu, Y. Bian, M. Yuan, C. Yang, Q. Meng, C. Chen, P. A. Ma and J. Lin, *Small*, 2023, **19**, 2207825.
25 Y. Liu, X. Wang, H. Chen, T. Wu, Y. Cao and Z. Liu, *ACS Appl. Mater. Interfaces*, 2023, **15**, 8937–8945.
26 Y. Fan, P. Xu, Q. Fang, Y. Zhu, F. Cao, Z. Zhao, D. Wu, X. Yang, D. Li and X. Liu, *ACS Appl. Mater. Interfaces*, 2023, **15**, 27183–27194.
27 G. Wang, Y. Su, X. Chen, Y. Zhou, P. Huang, W. Huang and D. Yan, *Bioact. Mater.*, 2023, **25**, 189–200.
28 H. Cheng, Y. He, J. Lu, Z. Yan, L. Song, Y. Mao, D. Di, Y. Gao, Q. Zhao and S. Wang, *J. Colloid Interface Sci.*, 2023, **639**, 249–262.
29 L. Sun, Y. Cao, W. Li, L. Wang, P. Ding, Z. Lu, F. Ma, Z. Wang and R. Pei, *Small*, 2023, **19**, 2300101.
30 S. Wu, C. Liu, W. Li, C. Zhang, D. Chen, C. Xu, L. Su and X. Wang, *J. Mater. Chem. B*, 2023, **11**, 2455–2465.
31 Q. Li, J. Yu, L. Lin, Y. Zhu, Z. Wei, F. Wan, X. Zhang, F. He and L. Tian, *ACS Appl. Mater. Interfaces*, 2023, **15**, 16482–16491.
32 H. Zhang and H. Zhang, *Light: Sci. Appl.*, 2022, **11**, 260.
33 J.-Y. Liu, N. Liu, Y. Wu, X.-M. Ning, W.-C. Zhang and J. Qian, *ACS Appl. Nano Mater.*, 2023, **6**, 270–282.
34 R. Cui, B. Li, C. Liao and S. Zhang, *Regener. Biomater.*, 2023, **10**, rbad021.
35 M. Ji, H. Liu, J. Gou, T. Yin, H. He, Y. Zhang and X. Tang, *Nanoscale*, 2023, **15**, 8948–8971.
36 J. Qi, G. Jiang, Y. Wan, J. Liu and F. Pi, *Chem. Eng. J.*, 2023, **466**, 142960.
37 Q. Xue, R. Kang, D. J. Klionsky, D. Tang, J. Liu and X. Chen, *Autophagy*, 2023, **19**, 2175–2195.
38 B. Zhang and R. Burke, *Metallomics*, 2023, **15**, mfad010.
39 S. Hou, Y.-E. Gao, X. Ma, Y. Lu, X. Li, J. Cheng, Y. Wu, P. Xue, Y. Kang, M. Guo and Z. Xu, *Chem. Eng. J.*, 2021, **416**, 129037.
40 Y. Bai, J. Zhao, L. Zhang, S. Wang, J. Hua, S. Zhao and H. Liang, *Adv. Healthcare Mater.*, 2022, **11**, 2102759.
41 X. J. Loh, S. J. Ong, Y. T. Tung and H. T. Choo, *Polym. Chem.*, 2013, **4**, 2564–2574.

